HIGHLY ENERGETIC ACTUATOR FOR HOPPING SCOUT-ROBOT FOR LUNAR GRAVITY - TEST RESULTS OF THE BREADBOARD MODEL

Łukasz Wiśniewski [(1)], Mateusz Przerwa [(1)], Jerzy Grygorczuk [(1)]

[(1)]*Astronika Sp. z o.o., ul. Bartycka 18, 00-716 Warsaw, Poland, Email:* lwisniewski@astronika.pl

ABSTRACT

This paper summarizes work on developing and testing two high-energy actuators for the Galago jumping robot. Considering the low power consumption required for lunar missions, we have focused on measuring jump efficiency factors. These can include mechanical efficiency resulting from the robot architecture, internal losses, and efficiency related to energy dissipation during the jump. This paper describes the context and requirements for the actuators, the rationale for selecting the robot architecture, a description of the actuator performance, and the results of jump performance tests for single-leg stands. The results confirm the actuators' robustness, high energy performance, and thus the applicability for a jumping robot. They allow confirming the estimation of jumps on the Moon from 3-6m depending on the type of surface for the proposed 10 kg robot. A method of utilizing energy dissipation coefficients to index surface properties while improving jump planning accuracy is also provided.

1. INTRODUCTION

1.1. Mission case and objectives

This research considers the development of a novel robotic platform called Galago for delivering scientific instrumentation for in-situ geomorphology studies and prospecting to the areas normally not accessible to rovers. It provides the scout capabilities that would significantly lower the risk of exploring undulated terrains during lunar missions (e.g., rough, and hardly accessible terrain, deep craters, including Permanently Shadowed Regions, lava tubes, steep slopes, and boulder fields).

The development is driven by the intensification of exploration programs, as outlined by multiple frameworks, e.g., *Lunar Exploration Roadmap*, *Strategy for Science at the Moon*, *Space Resources Strategy* or *Artemis Science Definition Report*, increasing the number and priorities of surface exploration objectives on the Moon and other bodies.

The project's objective is to provide a design applicable to a broad spectrum of mission scenarios. Therefore, we specifically designed Galago for the lunar environment, convenient since once solved for that gravity, the design could be utilized in lower- or microgravity cases. Consequently, we consider three lunar scenarios: round trip (e.g., providing reconnaissance for a mother lander or rover in the proximity of Rima Hadley area), long-term

and self-powered (e.g., area of Ina Caldera), and one-way in PSR (e.g., Shackleton crater). The specific objectives and constraints for such a system would include:

- addressing the mission risk (be capable of traversing various types of terrain);
- increasing the scientific return (possess volume for a dedicated payload);
- leveraging the added value by its relatively low cost, low-mass, low-power, and low-volume (accommodate to a variety of missions);
- provide modular, minimalistic, and robust configuration of the robot.

In the light of those objectives, we provide the current state of development of a critical sub-system: the actuator, the *muscle* of the robot. It refers to the previous studies described in [1], [2], and [3]. The possible payload configurations were discussed in [4].

1.2. State-of-the-art

There are several approaches to address the challenging task of planetary mobility systems. It is not a trivial task to suit a technology that would cover all those objectives. Often, they are tailored to a specific mission or require a certain system adaptability level. In the context of modularity and scalability of the system configuration to multiple mission scenarios, we can identify three groups of development:

1) tailored systems, not necessarily scalable to other environmental conditions (like microgravity hoppers: MASCOT, MINERVA [5], Hedgehog [6]; or Martian helicopter, Ingenuity, which is limited to an atmosphere);
2) adaptable systems with high autonomy and increased number of DoFs (Degree of Freedom). Agile and addressing majority of mission risk at cost of high-power consumption. Good examples are: Spacebok [7], or LEMUR 3 climbing robot [8];
3) scalable and modular systems e.g. AXEL, MoonDiver [9], or Galago, provide a minimalistic yet robust principle of operation that can suit various missions regardless of gravity and environmental conditions. Usually, low power but with limited controllability.

2. DESIGN JUSTIFICATION

2.1. Platform design rationale

In our research, we selected hopping as a primary locomotion principle since it allows for a relatively low

cost of transportation [10], high efficiency, only improves with reduced gravity and may overcome many planetary exploration obstacles, e.g., cliffs, dunes, and obstacles larger than the size of the platform.

To fulfill the minimalistic and robust design requirement, we focused on selecting a system architecture with only three actuated DoFs, the minimum needed to relocate in 3D space. There are known solutions for three DoFs of hopping systems, where the function is decomposed into wheels for roving and a separate actuator for hopping (e.g., Boston Dynamics Sand Flea robot or Small Hopping Rover [11]). Such solutions would not be fully scalable to any space mission as required since the traction would be minimal for micro-gravity due to weightlessness. Therefore, in Galago, we use a configuration of three identical actuators distributed around the disc casing.

In the scope of the project, we considered two actuation principles: linear one (described in [3]) and rotary one (described herein), Fig. 1.
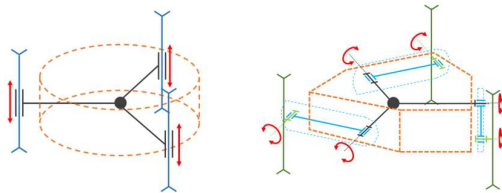

Figure 1. The trade-off between kinematic configurations of the actuating legs on the platform
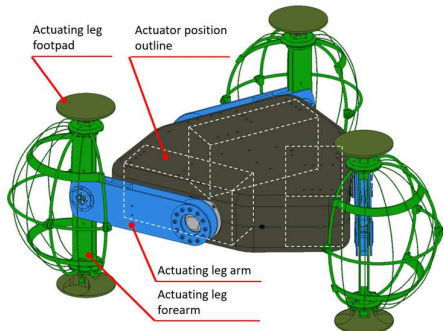

Figure 2. Galago isometric view with indicated location of the rotary actuators and details of the actuating legs

The rotary one has now become the baseline configuration – Fig. 2. The lesson learned behind shifting to the rotary one is the solution to the vectorization problem described in section 2.2 and strengthened by the need for modularity and ease of reconfiguration to more complex systems in the future.

The proposed architecture meets the objectives by taking advantage of the symmetrical design, reducing the DoF needed. It possesses a relatively low mass (less than 10 kg) and is always ready for the next jump regardless of which side it lands. Its sub-systems fit into a disc casing with a diameter of c.a. 40 cm, distributed along actuating legs are finished with a lightweight mesh protecting the interior against landing shock. We foresee at least three reconnaissance cameras, one on each side, and a dedicated total of 464 cm^3 volume for the scientific payload - Fig. 3.
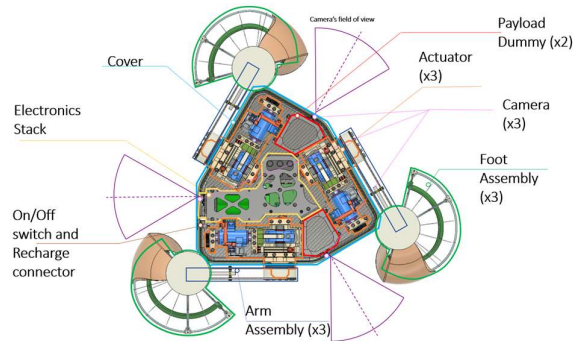

Figure 3. Top view over Galago robot showing interiors of the platform

The most intrinsic sub-system of the overall robot is its actuator with its actuating leg, which we focused on in the following sections.

2.2. Actuating legs and platform vectorization

The advantage of the rotary actuator results from the improvement of actuating leg design and performance of the overall platform. Specifically, it keeps the simplicity of the design since, without the need for additional actuators, it can provide a tangential component against the surface regardless of on which side the robot lands – see Fig. 4. Consequently, this creates the effective vectorization which was demonstrated via multibody analysis in MSC.Adams (Fig. 5).
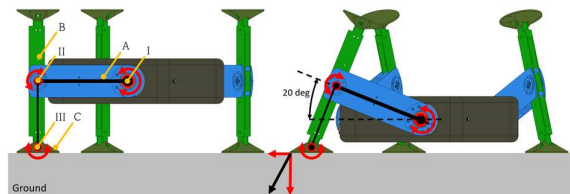

Figure 4. Rotary actuating legs and vectorization principle (symbols described in the text)

The implemented design consists of the main *arm* (A) driven directly by the rotary actuator (I) inside the platform. The *arm* is finished with a *knee* hinge (II) linked to the *forearm* link (B). The *forearm* link is connected to a *footpad* (C) via a free rotating and passive *ankle* hinge (III). The *knee* hinge is equipped with additional stiffness (i.e., spring) to provide enough torque to compensate for the weight of the platform but small enough to allow for a rotation of the links during take-off. Besides, the actuating leg's repelling function also protects the platform's payload against the landing shock.
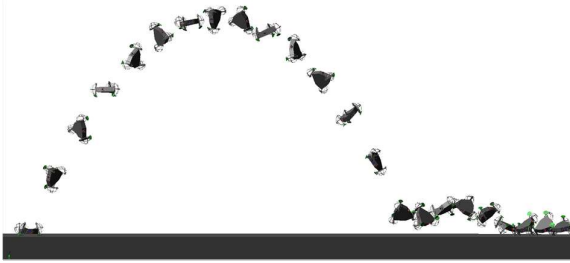
Figure 5. Multibody analysis demonstrating the robot's performance in lunar gravity

2.3. Actuator's design rationale

One of the most crucial parts of actuator's design is determining the means of energy accumulation. The literature considers flywheels, springs, or capacitors. The question is which of them is the most efficient? As shown in [12], direct drives that utilize the capacitor's energy possess a motor-specific limitation on the energy density per unit mass. Considering the flywheels or eccentric masses, they were used in various hopping robots, i.e., MINERVA, MASCOT, and Hedgehog. However, the flywheel inertia is not optimal for energy and momentum exchange in such a system. Therefore, we propose accumulating the energy in a set of springs, using a work performed by a low-power DC motor multiplied by the set of gear and a ball screw, which allows us to accumulate relatively high energy and use it directly to repel the surface.

Regarding the spring selection, the driving parameter for the actuator's design would be the required distance of the spring compression. Two extremes can be considered, compressing at large distances but using relatively small forces (and consequently with the extended time of operation), e.g. [12], [13], or using smaller distances at the expanse of increased forces – which we did for Galago. The first one requires large envelopes of operation to accommodate long linkages that need to fold and unfold. While the small forces are relatively easy to handle, this is occupied by the additional risk of exposing the mechanism to dust and sharp surfaces or blocking the movement of that parts by rocks which are more likely to land in between the linkages. Therefore, for the sake of robustness of the systems, we decided to compress the springs at relatively low distances with large forces, hence providing the ease of dust sealing, compact design, and reducing the risk of rock interruptions.

As mentioned earlier, we have breadboarded two actuators' models: linear one and rotary one. We described the linear one (Fig. 6) in more details in [3], and its principle of operation is shown in Fig. 7. The actuator provided valuable information about performance on various surfaces discussed in the following sections. However, it was descoped in favor of the rotary actuator for the reasons already provided.
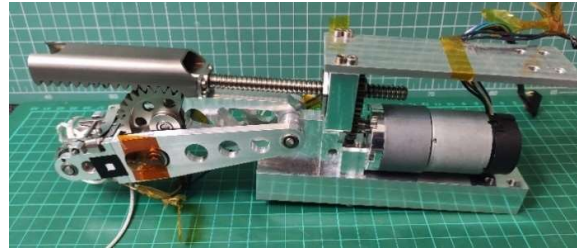

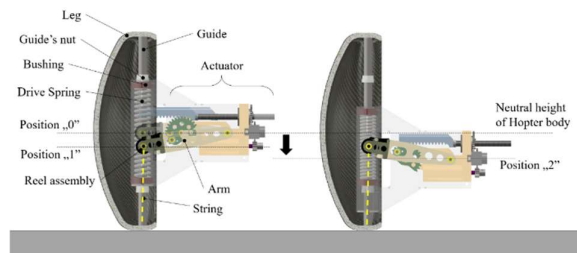Figure 6. The breadboard model of the linear actuator [3]

Figure 7. Visualization of the linear actuator in a neutral position (left) and tensioned (right) [3]

The rotary actuator is shown in Fig. 8 and Fig. 9, and its sequence of operation in Fig. 10. It consists of a few sub-assemblies: on the right, we see the central axis driven by a drum with a cam (blue), which compresses the drive springs (yellow) inside the drum. We see the trolley assembly on the left (grey), which is driven by a DC motor via gears and a ball screw on rails (orange). The trolley pulls the drum via the tether. There is a set of two independent locks actuated by electromagnets that release the tether at the desired angular position of the drum's axis (which corresponds to the specific energy of the drive springs). The maximum rotation of the drum is 20 deg, which translates to 16.9 mm of compression of the springs, which provides 7000 N of reaction force (and hence c.a. 60 J). Tab. 1 summarizes the parameters of the actuator.
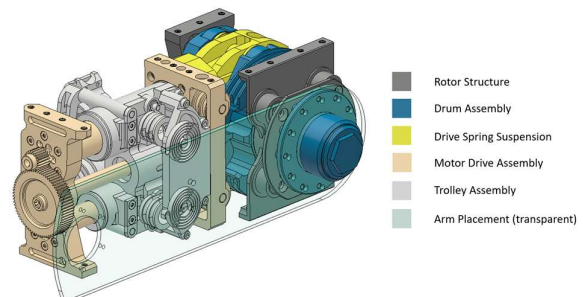

Figure 8. Subassemblies of the rotary actuator. Colours referenced in the text
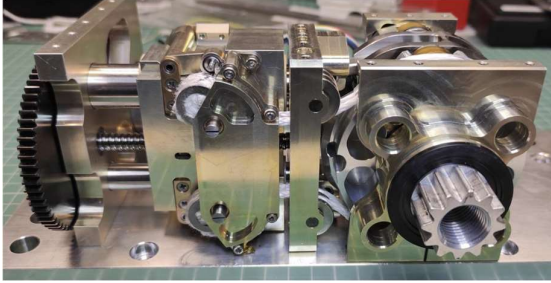
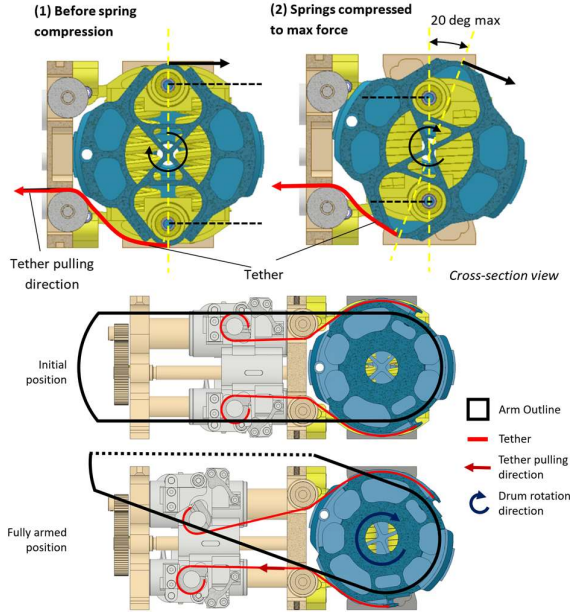Figure 9. The breadboard model of the rotary actuator

Figure 10. Operational sequence of the rotary actuator

Table 1. Rotary actuator's parameters

Description	Value
Actuator's Mass	1.5 [kg]
Actuator's Av. Power	4.5 [W]
Power settings	Any
Maximum operational cycle: - Loading - Return	94 [s] 91 [s]
Rotation angle	20 [deg]
Dimensions and Volume	195 x 115 x 82 [mm^3]
Accumulated energy	60 [J]
Energy per mass unit	40 [J/kg]
Actuating leg inertia vs. total inertia	21616 [kg/mm^2]/ 124993 [kg/mm^2] = 0.173
Actuating leg mass vs. total mass	1081 [g] / 9500 [g] = 0.114

3. ACTUATORS' TESTING

3.1. Methods and device under tests

We have proposed and validated a method for analyzing the performance of the hoppers actuator by comparing the input energies accumulated in the drive springs (E_{used}) with the effective potential energy of the robot at the apex of its hop: 1) actual one (E_{pot_test}); 2) and the one predicted from analysis ($E_{pot\_analysis}$). Also, we have demonstrated in [3] that the relations between those energy values constitute the following functional coefficients (indices) of hopping effectiveness:

- Coefficient of energy loss in the momentum exchange between the actuating leg and the platform (Eq. 1);
- Coefficient of energy loss in the mechanism's internal friction (Eq. 2);
- Coefficient of energy dissipation on the surface (Eq. 3).

$$C_1 = 1 - \frac{E_{pot_{analysis}}}{E_{used}} \qquad (1)$$

$$C_{2_{ref}} = 1 - \frac{E_{pot_{test}}}{E_{pot_{analysis}}} \qquad (2)$$

$$C_3 = 1 - \frac{E_{pot_{test}}}{E_{pot_{analysis}} \cdot \left(1 - C_{2_{ref}}\right)} \qquad (3)$$

As a next step, we have developed two test stands for testing the isolated uni-directional movement for each actuator. The tests were conducted in Earth gravity and under normal conditions.

The objective of the linear actuator test campaign was to validate its performance for various shapes and sizes of the footpad (a rounded one and flat ones with variable surface areas, Fig. 13) on four various surface types (listed later), and in the direction perpendicular to the surface. The linear actuator was mounted on a rotary arm which constrained its movement to a single plane. Additionally, knowing that the actuator also operates at an inclined angle, we tested its performance in a tilted configuration at a 20deg angle for a reference surface material (i.e., quartz sand), Fig. 11.

Figure 11. View of the testbed for the linear actuator [3]

The rotary actuator has been tested on a uni-directional rail system, constraining the hops to the linear up-and-down movement (Fig. 12). The objective of this test was to demonstrate the performance of the rotary actuator, especially in the context of the configuration with additional un-actuated DoF as described previously in section 2.2.
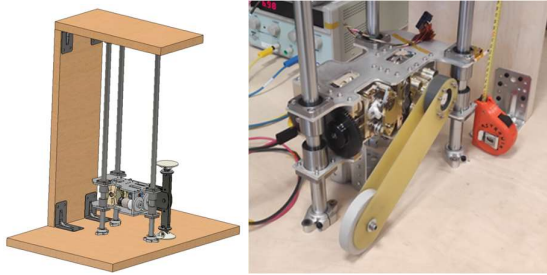
Figure 12. View of the testbed for the rotary actuator

3.2. Results and discussion

We have synthesized the essential results of the test campaign in this section. Some of those test results are described in more detail in previously published [3].

The in-built effectiveness of hops of the test models expressed by the C_1^*=1- C_1 index is, on average, 73% (loss index C_1=27%) for the linear actuator and 92% (C_1=8%) for the rotary actuator, which is very high compared to a few percent of microgravity and internally actuated hoppers [6]. The further increase of this efficiency can be achieved by consequently lowering the inertia of the actuating *arm*. We have also demonstrated relatively low friction losses (the C_2 index), i.e., values of 4.8% to 6% for the actuator.

We have measured the energy dissipation coefficient (C_3) for various footpad shapes and sizes on the reference surface (i.e., quartz sand) – Fig. 13. From the data, the actuator likely loses over 50% of the hopping energy if the footpad size is less than c.a. 40cm^2. For Galago hopping robot, we target a footpad size of at least 54cm^2 to ensure that the energy dissipation is limited and performance enhanced. Larger footpads are an asset but increase the *arm's* inertia and reduce the C_1 coefficient simultaneously. Therefore the optimal point needs to be found. The exemplary hopping using large footpad (configuration #4 with 257 cm^2 of the footpad area) is shown in Fig. 14 (slow motion).

We measured the energy dissipation coefficients for the selected 54cm^2 footpad size (the values apply to repelling perpendicularly to the surface):

- Highly cohesive material, regolith analog (i.e., Syar with a loose density of c.a. 2010 kg/m3), provides 7 – 31% of energy dissipation.
- Cohesionless material (i.e., quartz sand with grain size 0.5-1mm loose density of c.a. 1840 kg/m3): 29% – 48%.
- Rocks with high density (i.e., quartz aggregate, 1mm loose density of c.a. 1700 kg/m3 grain size 8-16mm): 4% – 19%.
- Porous rocks (expanded clay, loose density of c.a. 270 kg/m3): 40% – 53%.

Worth mentioning is that in the inclined test (20deg), the energy dissipation factor on quartz sand and the nominal footpad area size (54cm^2) were on average 1.5 times higher compared to the perpendicular case (i.e., the dissipation of energy C_3 was at the level of 51% – 69%). Although this value was measured for a specific configuration and materials, it can be treated as an indicator of the order of magnitude of the variations and possibly used as a scaling factor for other materials (further tests are needed, though).
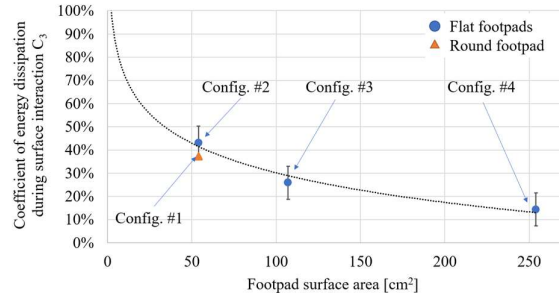

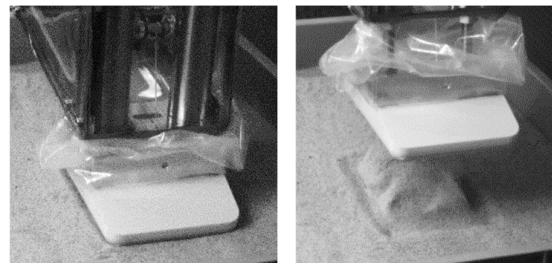Figure 13. Dependence of the coefficient of surface energy dissipation against footpad surface area [3]

Figure 14. Hop in quartz sand with the largest footpad [3]

Another observation impacting hopping and crawling robot control strategies was a rapid change of energy dissipation measured for cohesive regolith analog (i.e., Syar). Fig. 15 shows the energy dissipation coefficient measured for Syar, with a nominal footpad area of 54 cm^2 conducted in one place. The regolith demonstrated rapid densification, which reduced the dissipation coefficient almost two times after each hop in one place. This observation can be used as a motion planning strategy for the next hop, where the robot first probes the surface below itself via little hops and densifies it to reduce hopping uncertainty. Interestingly, this practice can be observed with animals that tend to wiggle their feet in place before making a large leap.
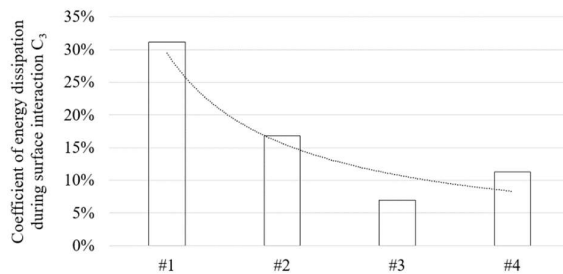

Figure 15. Results of the measurement of coefficient C_3 for subsequent jumps on Syar surface [3]

In the rotary actuator test campaign, we focused on demonstrating its efficiency, performance, and endurance. The tests consisted of runs using a slow-motion camera and capturing the angular and linear position of the 1-D platform and comparing it with the expected performance. The hopping height compared to the predicted one matched 94%. In Fig. 16, we see an example of free rotation tests.
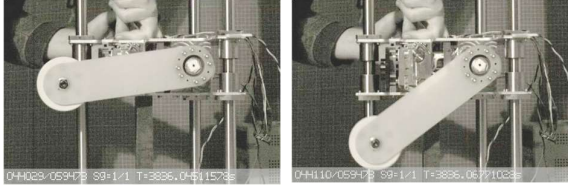

Figure 16. Free rotation test of the rotary actuator

One of the runs utilized a loading of the springs at their complete range (220Nm resulting in 60 J of accumulated energy) where we achieved good matching of the energy release and the observation of the uninterrupted oscillatory movement of the *arm* (95.2% of kinetic energy matching with analytical calculations).

Finally, we have also demonstrated the baseline functionality of the actuating leg, i.e., equipped with a single active DoF (the *arm*) and two passive ones: *knee* hinge and *ankle* of the foot hinge. Fig. 17 shows an exemplary sequence of operation of the actuating leg (slow motion). The *knee* hinge possesses an additional stiffness of between $0.5 - 1$ Nm/deg. The stiffness is explicitly tailored to provide additional support against the weight of the platform while allowing for free rotation of the *knee* hinge and producing the tangential force on the surface during the take-off.
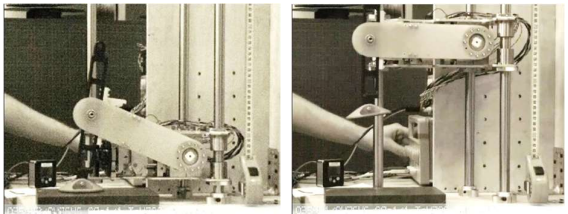

Figure 17. Hopping tests of the rotary actuator with actuating leg

4. IMPLICATIONS TO SYSTEM OPTIMIZATION AND CONTROL STRATEGIES

4.1. System optimization

By tailoring the multibody analysis model simulated on a rigid surface with the actual physical models on non-rigid surfaces, we have demonstrated that it is possible to calculate the expected performance (i.e., the height of jump) of the hopping robot without a need to implement sophisticated contact dynamics or modeling of granular matter. We simplified the analysis only for a specific case

of vertical hops, where the potential energy of the hopping robot (E_{pot}) equals a product of the introduced efficiency coefficients (C_1, C_2 and C_3) and the energy accumulated in the spring E_{spr} (subtracted by the energy coming from the weight of the robot E_{grav}, which is negligible considering large stiffnesses of the drive springs), Eq. 4:

$$E_{pot} = (1 - C_1)(1 - C_2)(1 - C_3)(E_{spr} - E_{grav})$$
$$= C_1^* \cdot C_2^* \cdot C_3^* \cdot (E_{spr} - E_{grav}) \quad (4)$$

From here, we can predict a maximum hopping height depending on the system mass (M), gravity (g), and various properties of the surface (Eq. 5):

$$h_{max} = \frac{E_{pot}}{Mg} = \frac{C_1^* \cdot C_2^* \cdot C_3^* \cdot (E_{spr} - E_{grav})}{Mg} \quad (5)$$

Exemplary optimization analysis of the robot's performance in lunar gravity as a function of its overall mass is provided in Fig. 18. It shows the expected height of a vertical jump, assuming the constant mass of the actuating legs (3kg) and constant hopping energy.
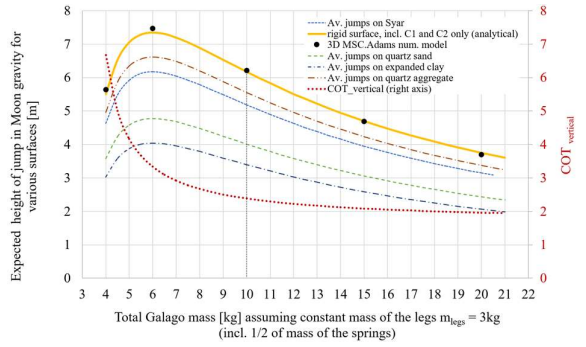

Figure 18. Expected maximum height of jump of Galago for various surfaces in Moon gravity. The X-axis is the total mass of the hopper, assuming the constant mass of the legs and drive springs

The plot also shows the calculated COT (Cost of Transportation coefficient). COT is a unitless coefficient interpreted as the energy consumed to move a unit weight a unit distance [10]. The coefficient can be used as a convenient optimization function to compare various forms of mobility regardless of the gravity in which it operates. The described tests and analysis focused only on vertical hops. Therefore, we calculated the COT for the maximum height of the jump (i.e., assuming relocation of the robot to a cliff or shelf). In such a case, the analysis is simplified, and by combining Eq. 5 and making the assumption that the energy consumed ($E_{consumed} = E_{spr}/C_0$) is the spring energy ($E_{spr}$) increased by a factor of electromechanical efficiency of the system (C_0), we can see that the $COT_{vertical}$ would depend only on system coefficients as in Eq. 6 (E_{grav} is negligible):

$$\text{COT}_{\text{vertical}} = \frac{E_{consumed}}{mgh_{max}} = \frac{1}{C_0^* C_1^* C_2^* C_3^*} \qquad (6)$$

For the given boundary conditions, assuming hopping on a rigid surface ($C_3 = 1$) and electromechanical efficiency of $C_0 = 0.67$, the 10-kilogram platform would have $\text{COT}_{\text{vertical}}$ equal to 2.4 or lower. However, the actual coefficient could be determined only on the full-scale model (the test set-up was not designed to determine the cost of transportation). For comparison, an intriguing synthesis of COTs is provided in [14], where the MIT Cheetah robot performs with a COT of 0.5, ASIMO robot has a COT of 2, and Boston Dynamics BigDog has a COT of 15.

A notable conclusion from the plot in Fig. 18 is that the COT decreases with the increased mass of the platform. At the same time, the highest performance (the highest jump) would be achieved for a platform with a total mass of 6kg. In other words, it is demonstrated that for the given assumptions, the higher masses of the platform may be more efficient from the cost of transport point of view, but not the performance. Therefore, each time a trade-off shall be done to either optimize for the highest performance (being able to maneuver against larger obstacles and descope the payload mass) or to maximize the payload mass but traverse with less agility.

From the plot, we can also see that for the targeted mass of Galago (10kg), the highest jump varies from 3 – 6m depending on the surface type.

4.2. Hopping accuracy and primary control strategies

We can use the previous method based on the described jump energy efficiency coefficients for an inverse analysis aimed at prediction and improving subsequent jumps' accuracy.

We assume a proportional relationship between the jump energy from these coefficients and the energy accumulated in the drive springs. Thus, one can use a simulation model of a robot jumping on a hard surface to determine the actual trajectory of the jump on a loose surface, using as input the numerical model's rescaled energy relative to that used according to this relationship as in Eq. 7:

$$E_{input} = C_2^* \cdot C_3^* \cdot E_{used} \qquad (7)$$

Based on a test campaign of 34 jumps on different surfaces, we performed an MEA analysis, which shows an average discrepancy between the planned and achieved jump of 7.6% (derived from Fig. 19), which is relatively insignificant considering the small number of trials. Measurements were made on the previously described 1-D testbeds.

As a result, we propose an algorithm for planning the next move for a jumping robot decomposed into 2 phases [3]:

Calibration Phase:
1. Identify masses and inertias of the actual robot.
2. Prepare a numerical model matching the inertias and ideal actuating forces. Omit the losses and uncertainties. Determine C_1 as per Eq. 1.
3. Conduct vertical hops on rigid surface. Determine C_2 as per Eq. 2.

In-field Phase (Recurrent):
4. If needed, conduct vertical hops on the uncertain surface. Determine C_3 as per Eq. 3.
5. Recalculate C_3 for the lateral hop.
6. The numerical model calculates the possible hopping envelope for the next hop based on the recalculated C_3. Use the scaled energy model to input the numerical one (Eq. 7).
7. Select the target inside the envelope and tension the springs according to the required energy level.
8. Perform the hop.
9. Self-localize. Return to step 4.

To implement this algorithm, we expect that it is possible to use sensors that already exist onboard the robot, thus saving mass on the payload. The required sensing reduces to:
- Actuators input energy, controlled by measurement of a deflection of the springs;
- The effective kinetic or potential energy of the hopping system can be determined by either measurement of the height of the jump (as done here but maybe tricky for planetary application) or the time of travel between actuators trigger and the first contact with the ground (i.e., by monitoring internal accelerometer). The latter is sufficient since the physics of projected vertical motion is well known.
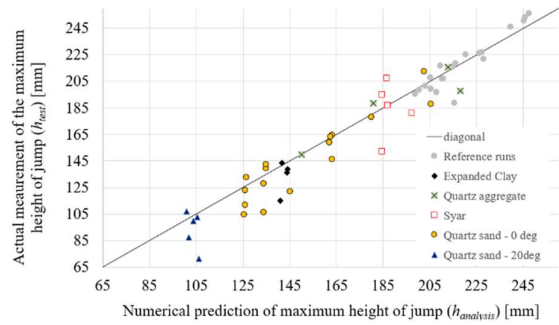

Figure 19. Test measurements (h_{test}) compared to predicted height of jump from analysis ($h_{analysis}$) [3]

5. CONCLUSIONS

The article's key message is that we have demonstrated the functionality of the breadboard models of two actuators, a linear one and a rotary one, both applicable for space hopping robots. Satisfactory matching results were achieved between the numerical models and their physical representations. Due to modularity constraints,

the rotary one can be broader used in future lunar missions.

The proposed actuator takes advantage of slow energy accumulation, allowing low power consumption and significantly increasing energy capacity. The proposed architecture considers the low inertia of the actuating leg to achieve the system's high efficiency by directly repelling from the surface (the efficiency coefficient C_1^* expected in range 60%-80%). We have demonstrated and measured the actual surface area needed to repel from the surface of various representative analogs and concluded that for surface areas below 40cm^2, the energy dissipation (C_3) likely increases to values greater than 50%. It is beneficial to provide a surface area of larger values.

We have also demonstrated via analysis that it is possible to use a minimum of three actuators to vectorize the hopping trajectory. However, it is necessary to ensure the clearly defined tangential force to push away from the surface. In such a case, slippery effects may occur, and we have measured that at an angle 20deg on quartz sand, the energy dissipation losses may increase by 1.5 times more than the one conducted perpendicularly to the ground. This value should be considered indicative only since the indices undoubtedly vary on the properties of pair foot-regolith. Consequently, we can confidently forecast that our 10kg platform equipped with the actuators could hop in lunar gravity as high as 3-6m during its vertical hops depending on the surface type.

We have also demonstrated a recurrent algorithm. We can use simplified contact dynamics modeling (avoiding analysis of grain interaction) and implement the indices that scale the input energy accordingly to predict the hopping result and include it in the next hop. As a result, the robot can characterize the ground during its traverse while improving its movement accuracy by those indices. The method may enhance hopping robots' control strategies in general.

6. ACKNOWLEDGMENTS

7. REFERENCES

1. Wisniewski L., et. al.; Mobility and terrain accessibility analysis for Hopter—An underactuated mobile robot for planetary exploration. In Proc. of the ASTRA 2017, Leiden, The Netherlands, 20–22 June 2017

2. Wisniewski L., et. al.; Design Features of Novel High Energy Impulsive Drive of Underactuated Mobile Robot for Planetary Exploration. In Proc. of the 17th ESMATS, Hatfield, UK, 20–22 September 2017.

3. Wisniewski L., et. al.; Energy Dissipation during Surface Interaction of an Underactuated Robot for Planetary Exploration. Energies 2021, 14, 4282. https://doi.org/10.3390/en14144282

4. Mège, D. et. al.; The Highland Terrain Hopper (HOPTER): Concept and use cases of a new locomotion system for the exploration of low gravity Solar System bodies. Acta Astronaut. 2016, 121, 200–220.

5. Lange C., et. al. Micro- and nanolander on the surface of Ryugu – Commonalities, differences and lessons learned for future microgravity exploration, Planetary and Space Science, Vol. 194, doi: 10.1016/j.pss.2020.105094.

6. Hockman B., et. al.; Design, Control, and Experimentation of Internally-Actuated Rovers for the Exploration of Low-gravity Planetary Bodies. Journal of Field Robotics, 34(1), 5–24. doi:10.1002/rob.21656

7. Kolvenbach H., et. al.; Towards Jumping Locomotion for Quadruped Robots on the Moon. 2019 IEEE/RSJ International Conference on Intelligent Robots and Systems (IROS). doi.org/10.1109/IROS40897. 2019. 8967552

8. Parness, A., et. al. LEMUR 3: A limbed climbing robot for extreme terrain mobility in space. 2017 IEEE International Conference on Robotics and Automation (ICRA). Doi:10.1109/icra.2017. 7989643

9. Nesnas, I.A., et. al. Moon Diver: A Discovery Mission Concept for Understanding the History of Secondary Crusts through the Exploration of a Lunar Mare Pit. In Proceedings of the 2019 IEEE Aerospace Conference, Big Sky, MT, USA, 2–9 March 2019

10. A. D. Kuo. Choosing Your Steps Carefully. IEEE Robotics Automation Magazine, vol. 14, no. 2, pp. 18-29, 2007.

11. Maeda T., et. al. Design of shoe plate for small hopping rover on loose soil. 2018 IEEE Aerospace Conference. doi:10.1109/aero.2018.8396530

12. Hawkes, E.W., Xiao, C., Peloquin, RA. et al. Engineered jumpers overcome biological limits via work multiplication. Nature 604, 657–661 (2022). https://doi.org/10.1038/s41586-022-04606-3

13. Macario-Rojas A., et. al. CLOVER Robot: A Minimally Actuated Jumping Robotic Platform for Space Exploration. arXiv:2201.04171.

14. S. Seok, et. al. Design Principles for Energy Efficient Legged Locomotion and Implementation on the MIT Cheetah Robot. IEEE/ASME Transactions on Mechatronics, vol. 20, no. 3, p. 1117–1129, 2015.